Nickel nanoparticles supported on doped graphene-based materials for the ORR and HER in alkaline medium

Sthephanie J. Martínez [a], Alessandro Lavacchi [b], Enrico Berreti [b], Laura Capozzoli [b],
Claudio Evangelisti [c], Antonio Arranz [d], José Luis Rodríguez [a], Elena Pastor [a],*

[a] Instituto de Materiales y Nanotecnología, Departamento de Química, Universidad de La Laguna, PO Box 456, 38200 La Laguna, Santa Cruz de Tenerife, Spain
[b] Istituto di Chimica dei Composti Organometallici-Consiglio Nazionale delle Ricerche, Via Madonna del Piano 10, 50019 Sesto Fiorentino, Firenze, Italy
[c] Istituto di Chimica dei Composti Organometallici-Consiglio Nazionale delle Ricerche, Vias G. Moruzzi 1, I-56124 Pisa, Italy
[d] Universidad Autónoma de Madrid, Departamento de Física Aplicada, C/ Francisco Tomás y Valiente 7, 28049 Madrid, Spain

ARTICLE INFO

ABSTRACT

In this work, Ni nanoparticles (NPs), with nominal metallic loading of 20 wt%, were deposited on graphene-based materials (GMs) doped with nitrogen and sulphur, in order to study their electrocatalytic activity towards the oxygen reduction reaction (ORR) and hydrogen evolution reaction (HER) in alkaline medium. Different chemical reducing agents were employed to synthesize the catalysts. Results indicate that the presence of heteroatoms in the GMs influences the activity of both the GMs and the Ni-based catalysts. Thus, best results were obtained for catalyst containing nitrogen and sulphur for the ORR which favours the direct four-electron pathway, whereas for the HER, the highest performance was observed for *N*-doped materials.

1. Introduction

As the limited availability of conventional fossil fuels becomes more apparent, the world needs to shift to more sustainable and renewable sources of energy. Thus, the development of fuel cells (FCs) or electrolysers, energy conversion technologies devices that provide clean energy (renewable and environmentally friendly), essential to compensate for the expected shortage, has become key to achieving a solution to this problem [1]. Indeed, significant progress has been made in understanding the underlying mechanisms and catalysts that drive both the oxygen reduction reaction (ORR) [2–5] and hydrogen evolution reaction (HER) [6–9] that occur in these devices, leading to notable advances in these technologies. The current goal is to improve its efficiency, scalability, and economic viability, thus paving the way for the widespread adoption of hydrogen as a clean and sustainable energy vector. Today, critical raw materials (CRM) continue to have significant importance in the European economy. These materials, deemed strategically vital and with a high supply risk, are crucial for countless sectors such as electronics, renewable energy, automotive and aerospace, among others [10]. Thus, extensive research [11–16] has been conducted for decades to avoid the use of platinum group materials as catalysts for proton exchange membrane fuel cells (PEMFCs) and PEM electrolysers.

The slow kinetics of the ORR is one of the main constraints of PEMFCs [1,17,18]. To alleviate this problem, extensive research has demonstrated that doping graphene with heteroatoms such as B, P, N or S improves the catalytic activity of the catalyst, favouring the reaction through the 4-electron pathway. Soo et al. [19] studied the influence of different nitrogen precursors (melamine and urea) on the performance towards ORR and stated that those *N*-doped graphene oxide samples reduced with melamine exhibited higher current density and better activity. Later, Chanda et al. [20] prepared a nitrogen-doped graphene oxide using a microwave plasma technique with ammonia flow, developing an onset potential of 0.8 V_{RHE} towards the ORR. Furthermore, descriptions of the synergetic effect of double doping in graphene-based materials (GMs) can be found in the literature, more specifically, those related to S and N on the ORR activity [5,21–24].

Additionally, non-precious metals supported on GM catalysts can improve the catalytic activity towards ORR in alkaline medium [25,26]. For example, the insertion of NiCuP nanotubes and NiCuN nanorods into reduced graphene oxide (rGO) revealed a good catalytic performance through 4-electron pathway [27]. Zhang et al. [28] reported the synergetic effect between transition metal oxides and graphene-based materials, establishing that the incorporation of N heteroatoms indeed enhances the activity of these catalysts, leading to an onset potential for

the ORR of 0.89 V V_{RHE} and ca. 4-electron transfer number.

Regarding the HER, Ni-based catalysts, such as Ni-foam based [29–31] or Ni-Co alloys [32,33], stand out among others for their low cost, abundance, and outstanding activity towards this reaction in alkaline medium. Ni-graphene has also been proposed as catalyst for this reaction. Franceschini and Lacconi [34] reported an onset potential of -0.55 V_{RHE} for the HER at the Ni/rGO hybrid material prepared by electrodeposition. Nickel loaded graphene-like carbon sheets prepared by Xu and co-workers [35] showed an overpotential of -0.205 V V_{RHE} at a current density of 10 mA·cm^{-2}, whereas *N*-NiO nanosheets arrays reported by Wang et al. [36], and *N*-doped graphene-encapsulated Ni-Cu alloy from Liu and coworkers [37], presented values of -0.154 V and -0.122 V at the same current density, respectively.

In the present paper, GMs doped with N and S were synthesized employing caffeine and ammonium thiocyanate, both as doping and reducing agents, to study their electrocatalytic activity towards the ORR and the HER. In addition, undoped rGO was prepared following a hydrothermal method using sodium citrate as a reducing agent [38]. Finally, Ni nanoparticles were supported on graphene-based materials, considering a nominal metallic loading of 20 wt% by the sodium borohydride method.

2. Experimental

2.1. Synthesis of catalysts

2.1.1. Synthesis of graphene oxide (GO)

The preparation and physicochemical characterisation of GO have been already described in a previous work [5], following the reported modified-Hummers method [39]. Briefly, 1 g graphite powder ($<$20 μm, powder synthetic; Sigma-Aldrich) was mixed with 30 mL of concentrated H_2SO_4 (Merck P.A) cooled in an ice bath. Later, 3.5 g of $KMnO_4$ (99–100.5 %, Sigma-Aldrich) was slowly added while being continuously stirred and cooled. After removal from the ice bath, the mixture was stirred for 1 h at 35–40 °C. Then, the solution was diluted with 52 mL of Milli-Q and heated up to 95–98 °C over 15 min. Next, 140 mL of ultrapure water (18.2 M Ω cm^{-1}, Milli Q, Millipore) was slowly introduced, followed by 1.25 mL of 30 % v/v H_2O_2 (35 %, Emplura®), and the stirring was kept for 24 h. Finally, the dispersion was centrifuged with Milli-Q water until a pH of 7 was achieved in the supernatant liquid. The resultant GO material was dried using an oven at 60 °C overnight.

2.1.2. Synthesis of rGO using a green method

In order to obtain the rGO [38], an adequate amount (16.3 mmol) of reducing agent ($Na_3C_6H_5O_7$·$2H_2O$; $\geq$ 99.0 %, Sigma-Aldrich) was dissolved in Milli-Q water (40 mL) and mixed with 40 mL of GO aqueous dispersion (4 mg·mL^{-1}). The final dispersion was placed into a Teflon-lined autoclave and heated at 95 °C for 10 h. Afterwards, rGO was washed by centrifugation (4000 rpm, 10 min) using Milli-Q water and then transferred to an oven at 60 °C for 24 h to obtain a reduced GO powder.

2.1.3. Synthesis of doped GMs

The preparation of doped GMs with N and S/N has been already described in a previous work [5]. Concisely, an adequate amount (4 mmol) of reducing agent (NH_4SCN or caffeine) was ultrasonically dispersed in Milli-Q water and mixed with a GO aqueous dispersion (0.15 g·mL^{-1}) in each case. The final dispersion was placed into a Teflon-lined autoclave and heated at 160 °C for 10 h. Afterwards, SNrGO (from NH_4SCN; 99.99 %, Fluka) and *N*-rGO (from caffeine; $\geq$ 99.0 %, powder, Sigma-Aldrich) were washed by centrifugation using Milli-Q water and then transferred to an oven at 60 °C for 24 h to obtain a reduced/doped GO powder.

2.1.4. Ni-based catalysts preparation

The sodium borohydride reduction method (BM) [40,41] was used to reduce the metal precursor ($NiCl_2$·$6H_2O$; $\geq$ 98.0 %, Fluka). Briefly, an aqueous solution of the GMs was sonicated for 30 min and kept stirring for ca. 24 h. After that, a water solution containing the metal precursor was slowly added to the carbon suspension, and then, the pH was adjusted to 5 with diluted HCl solution ($\geq$37 %, Fluka) and kept under stirring for 24 h. Next, metal ions were reduced by the gradual addition of a $NaBH_4$ (99 %, Sigma-Aldrich) solution under sonication at a constant temperature of 20 °C and kept under stirring for 12 h. Subsequently, catalysts were copiously washed with ultrapure water under centrifugation (4000 rpm for 10 min). Finally, the material was submitted to a thermal treatment during 2 h under a reducing atmosphere (N_2:H_2 ratio of 95:5; 100 mL·min^{-1}) at 500° C.

2.2. Physicochemical characterisation

X-ray diffraction (XRD), scanning electron microscopy (SEM) coupled with energy dispersive X-ray technique (EDX), elemental analysis, Raman and infrared spectroscopy techniques were used to characterise the materials.

SEM images were obtained with a Zeiss Evo 15 microscope coupled with Oxford X-MAX (50 mm^2) EDX detector.

High-resolution transmission electron microscopy (HRTEM) images were acquired using a Thermofisher Talos F200X G2 at an accelerating voltage of 200 kV using a high speed CETA camera operating at a resolution of 4096 x 4096 pixels without any objective aperture. High angle annular dark field (HAADF) images were acquired with a Panther annular STEM detector using a convergent beam with an angle of 10.5 mrad and a camera length of 330 mm. The EDX maps were taken with a Super X spectrometer equipped with four 30 mm^2 silicon drift detectors with a collection angle of 0.7 srad. Data processing and arrangement have been performed with the Thermofisher proprietary software VELOX.

Powder XRD diffractograms were acquired from a X'Pert PRO X-ray diffractometer (PANalytical) to determine the crystal structure. Measurements were obtained using the CuK radiation ($\lambda = 1.5405$ Å) and the X'pert high score plus diffraction software. 2θ data were collected from 5° to 100° with a scanning rate of 0.04 s^{-1}. Crystalline phases were identified by comparing the experimental diffraction patterns with the Joint Committee on Powder Diffraction Standards (JCPDS).

An elemental analysis with an experimental error close to 0.04 % was performed using an Elemental Analyzer CNHS FLASH EA 1112 (Thermo Scientific).

Raman spectra were collected using a SPELEC RAMAN (Metrohm DropSens) microscope, with a green laser ($\lambda = 532$ nm) and a Raman probe in the 200 to 3200 cm^{-1} range. The equipment was controlled employing DropView Spelec 3.2.2 software. Infrared measurements were acquired with a JASCO FT/IR-6800 Spectrometer.

X-ray photoelectron spectroscopy (XPS) spectra were acquired using a hemispherical analyser equipped with five channeltron detectors (SPECS Phoibos 100 MCD-5). The Al Kα radiation (hν = 1486.6 eV) of a twin-anode X-ray source operated at 300 W was used. The base pressure in the analysis chamber was below $4·10^{-9}$ mbar during spectra acquisition. Binding energies were determined by referencing the C1s peak of C—C species at 284.6 eV. Data analysis and quantification were performed using CasaXPS software.

2.3. Electrochemical characterisation

The activity of the electrocatalytic materials was evaluated towards the ORR and HER using by means of cyclic voltammetry, linear sweep voltammetry and rotating ring-disk electrode (RRDE).

The electrochemical experiments were carried out at room temperature using a three-electrode half-cell, with a carbon cylinder as counter electrode and a hydrogen reference electrode in the electrolyte solution

(reversible hydrogen electrode, RHE) as reference. All the potentials in this work were given against the RHE. The working electrode consisted of a thin layer of the catalyst deposited onto a glassy carbon disc (0.196 cm^2). The ink was prepared by mixing 2 mg of the catalyst powder, 15 μL of Nafion® solution (5 wt%, Sigma-Aldrich) and 500 μL of Milli-Q water and keeping under sonication for 45 min. Electrochemical measurements were performed with a PC-controlled Autolab PGSTAT30 potentiostat–galvanostat (Metrohm Autolab) in 0.1 M NaOH (≥99.99 %, Sigma-Aldrich) electrolyte solution.

ORR studies in alkaline medium were performed using a rotating ring-disk electrode (RRDE, PINE) in the potential range from 1.1 to 0 V at 2 mV·s^{-1}. The potential at the Pt ring was kept at 1.2 V. Before each measurement, Argon (N50) was bubbled through the solution to avoid dissolved oxygen, and several cyclic voltammograms were performed in the potential range 1.0 – 0 V at a scan rate of 20 mV·s^{-1} for electrode activation. Then, for the ORR, the electrolyte was saturated with O$_2$ (99.995 %, Air Liquide) over 20 min at a controlled disk potential of 1.1 V. Steady-state polarization curves were carried out between 1.1 and 0 V at rotating speeds of 400, 600, 900, 1600 and 2000 rpm to evaluate the ORR kinetic parameters.

For the HER studies, the measurements were performed with a Princeton Applied Research (PARSTAT 3000A-DX, model 636A) potentiostat/galvanostat with a standard 3-electrode system, using RHE as reference electrode, a Pt-wire as counter electrode and rotating ring-disk electrode (RRDE) as working electrode (0.2475 cm^2). The ink was prepared following the same procedure as the above-mentioned. Higher electrolyte concentration was used to avoid significant resistance values. Prior to all the electrochemical studies for these reactions, the NaOH 1 M solution was first purged for 30 min with N$_2$ and then saturated with H$_2$ for 30 min. The potential was iR corrected to remove ohmic loss across the electrolyte. For the HER, polarization curves were carried out between 0.15 and −1 V at a scan rate of 2 mV·s^{-1}, with a rotation speed of 1600 rpm. Tafel analysis was performed by plotting the logarithm of current density (mA·cm^{-2}) vs. overpotential.

Hydrogen evolution reaction was also evaluated through electrochemical impedance spectroscopy (EIS) technique, performed at frequency range of 100 kHz to 0.1 Hz with a sinusoidal potential difference of 30 mV. EIS measurements were carried out using an OrigaFlex – OGF01A potentiostat–galvanostat from Origalys, controlled by OrigaFlex 5.0 software.

3. Results and discussions

3.1. Physicochemical characterisation

3.1.1. Graphene supporting materials (GMs)

First, graphene materials were characterized by XRD. Diffraction patterns of graphite, GO, rGO and two different doped GMs (*N*-rGO and SNrGO) are given in Fig. 1. Graphite develops a sharp peak located at 26.6° corresponding to the diffraction plane C(0 0 2). After oxidation, the graphitic peak shifts to 2θ = 10.9° which accounts for an increase in the interlayer spacing between the GO sheets. When GO is reduced (rGO, *N*-rGO or SNrGO), the number of intercalated oxygen functional groups (OFGs) decreases, appearing a broader contribution at 24-25°. Additionally, these graphene materials reveal a small signal close to 45°, associated to the plane C(1 0 0).

Diffraction parameters obtained from Fig. 1 are summarized in Table S1. The number of layers for all GMs was calculated using equation S1, ranging between 4 and 10 for the rGO materials, which allows us to expect that all prepared materials behave as graphene rather than graphitic materials (as stated in the literature [42,43], having more than 10 layers of graphene makes it behaves as bulk graphite). It is also shown that the C—C interplanar spacing expands from 0.34 nm for graphite to 0.88 nm for GO (with intermediate values close to 0.40 for the other reduced materials), which can be related to the presence of OFGs and other heteroatoms between the graphitic layers. According to the interplanar spacing from XRD results (Table S1) and confirmed by elemental analysis (Table S2), the amount of OFGs increases in the following order: SNrGO < *N*-rGO < rGO < GO. Considering the presence of both S and N (bigger than O atoms) in SNrGO, interplanar spacing for this material is higher than *N*-rGO, but lower than rGO and GO due to the higher amount of oxygen groups in these materials (*N*-rGO < SNrGO < rGO < GO).

Additionally, infrared spectroscopy allows to determine the nature of the functional groups present in the synthesized materials. The FTIR spectra obtained for graphite, GO, rGO, *N*-rGO and SNrGO samples and the assignment of the vibrational modes can be seen in Figure S1 and Table S3 [44–46]. Briefly, the FTIR spectrum of GO shows a broad band between 3600——2900 cm^{-1} and a peak at 1045 cm^{-1} that clearly indicates the presence of –OH groups, whereas the peak at 1725 cm^{-1} corresponds to the ketone (C=O) stretching vibration. The contribution
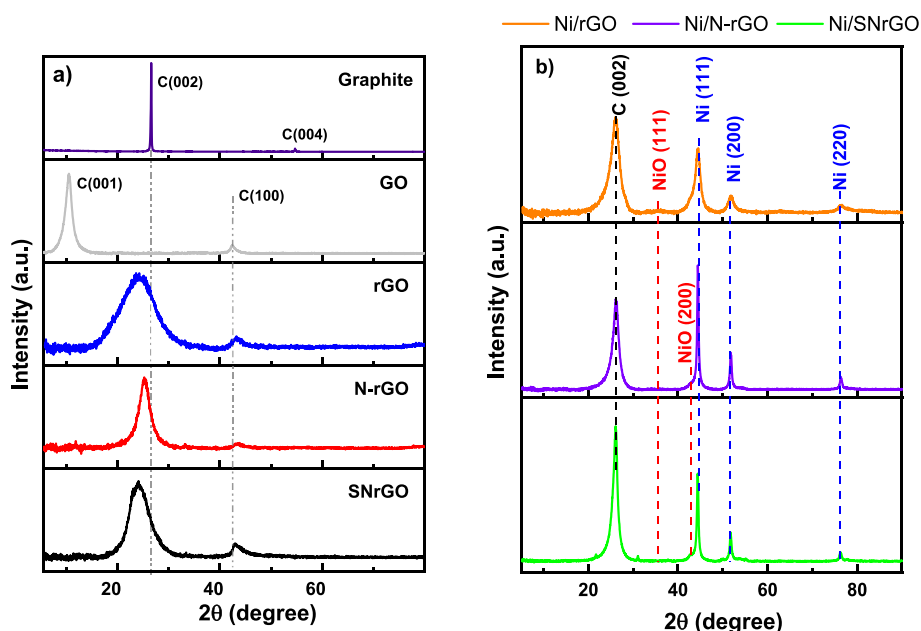

Fig. 1. XRD patterns for a) supporting materials and b) Ni-based catalysts.

at 1620 cm^{-1} can be assigned to the sp^2 hybridization (C=C) and that at 1220 cm^{-1} to C—O—C stretching mode. After the reduction, the intensity of all the signals diminishes, confirming that the reduction of the OFGs in the graphene oxide (C=O, –OH) is successfully achieved. In *N*-rGO and SNrGO, the small signals at 1640 and 1560 cm^{-1} correspond to the –NH$_2$ and –N—H stretching modes, respectively. The presence of S in SNrGO was confirmed by C—S signals at 1385 cm^{-1}.

On the other hand, Raman spectroscopy was employed to study the structural changes and the disorder degree, by comparing the intensities of the D (ca. 1340 cm^{-1}) and G (ca. 1580 cm^{-1}) bands. Low I$_D$/I$_G$ values are related to more graphitic systems (prevailing sp^2 domains) and high values with more disordered structures (with the presence of sp^3 hybridization) [47]. Fig. 2 depicts the Raman spectra for all the GMs.

Main results indicate an increase in the I$_D$/I$_G$ ratio (~1) following the order rGO < *N*-rGO < SNrGO when compared to graphite (I$_D$/I$_G$ = 0.22) and GO (I$_D$/I$_G$ = 0.86) which results from the increment in the relative presence of defects [48] in the structure, that is, the introduction of heteroatoms in the reduced GO. The presence of both C—S and C—N bonds in SNrGO points out the prevalence of sp^3 domains in this catalyst.

3.1.2. GMs containing Ni nanoparticles (NPs)

SEM coupled with EDX was employed to study the morphology, as well as Ni content, of the as-prepared Ni/rGO, Ni/*N*-rGO and Ni/SNrGO catalysts. Figure S2 depicts SEM images of the three different graphene materials with Ni NPs. A layered structure, with wrinkled ending sheets entangled with each other, can be seen. Ni content in the as-prepared materials (Ni/rGO, Ni/*N*-rGO and Ni/SNrGO) are 12.8, 20.6 and 18.7 wt%, respectively (Table S4), notably increasing its content when N and S are present in the graphene network for the supporting material (3.8 wt% N for *N*-rGO and 2.0 wt% S and 1.2 wt% N for SNrGO), which

Fig. 2. Raman spectra for all the materials studied.

indicates that the presence of heteroatoms could act as anchoring sites [49,50], leading to higher metal loading.

EDX analysis show that the carbon content in these samples is quite high (69–79 wt%) which interfere with N detection through overlapping of signals, which would make them impossible to be differentiated. Elements of low atomic number (such as N) are difficult to be detected through this technique, especially when they are present in lower quantities [51]. Thus, EDX failed to reliably demonstrate the presence of N. However, N content was nonetheless detected in Ni/*N*-rGO by elemental analysis (1.4 wt%). It has to be taken into consideration that the preparation of Ni-based catalysts involved a thermal treatment, which could be the reason for the decrease observed in S content in Ni/SNrGO (Table S4) compared with SNrGO (Table S2) and also the decrease in N content obtained from elemental analysis for Ni/*N*-rGO respect to *N*-rGO.

Ni nanoparticles distribution and surface topography were established by HRTEM, and results are depicted in Figure S3. HRTEM images confirm the presence of Ni NPs formation onto the graphene sheets. In general, a certain degree of aggregation of Ni NPs was observed, but this is lower in Ni/SNrGO (Figure S3 C), suggesting that the presence of both S as dopant heteroatom favours a good dispersion on the graphene material. Particle size for these materials was determined from HRTEM, having the results compiled and represented in a histogram (Figure S4). An asymmetric distribution can be seen for Ni/*N*-rGO, with a predominance of particles larger than average. The average particle size increases as follows: Ni/rGO (8.3 nm) < Ni/SNrGO (14.4 nm) < Ni/*N*-rGO (16.2 nm). Particle sizes are very similar to crystallite sizes (Ni/rGO (7.4 nm) < Ni/SNrGO (14.3 nm) < Ni/*N*-rGO (16.0 nm) from Table S5) and follows the same trend of Ni content (Ni/rGO (12.8 wt%) < Ni/SNrGO (20.6 wt%) < Ni/*N*-rGO (18.7 wt%) from Table S4) indicating that the amount of Ni is the factor determining these sizes.

HAADF and STEM coupled with EDX mapping were used to study the elemental distribution in Ni-based catalysts (Figure S5). The analysis shows that the O atoms are well distributed in the graphene support, also following the same pattern as Ni NPs and S in their respective counterparts.

Diffractograms for the Ni-containing catalysts are given in Fig. 1. Three peaks appear at 2θ = 44, 52 and 76° which are assigned to the (1 1 1), (2 0 0) and (2 2 0) crystallographic planes of fcc Ni NPs (JCPDS #04–0850). Meanwhile, XRD peaks at 37, 43 and 63° are related to the (1 1 1), (2 0 0) and (2 2 0) crystallographic planes of NiO (JCPDS #044–1159). Therefore, the presence of both crystalline Ni and NiO is established from these results. The Ni NPs crystallite size was determined from XRD patterns in Fig. 1 using the Scherrer equation (Table S5). Similar values were obtained increasing in the following sequence: Ni/rGO (7.4 nm) < Ni/SNrGO (14.3 nm) < Ni/*N*-rGO (16.0 nm) with an interplanar distance Ni-Ni of 0.18 nm calculated from the Ni (2 0 0) signal. The XRD crystallite sizes are similar to those particle sizes determined by HRTEM.

Additionally, the interplanar spacing for the carbon layer is the same in all cases (0.34 nm) and smaller than the corresponding graphene-supporting material, a result that can be ascribed to the decrease in O content that occurs after the introduction of the Ni particles (compare data for atomic % content in O in Table S2 and Table S4 for supporting GMs and Ni-containing materials, respectively). On the other hand, an increase in the number of graphene layers once N or S/N was inserted seems to be related to the content of N (3.8 and 1.2 N wt. % for *N*-rGO and SNrGO, respectively, see Table S2), which promotes the anchoring of Ni NPs (20.6 and 18.7 Ni wt. % for *N*-rGO and SNrGO, respectively) compared to those supported on rGO (12.8 Ni wt. %)(see Table S4). According to the results, the broadening of the diffraction peaks points out to a decrease in particle size (Table S5).

The disorder degree, according to the Raman spectra for the Ni-containing materials in Fig. 2, increases in the same order described previously for the supporting GMs. I$_D$/I$_G$ values for the metallic catalysts are higher than their respective supporting GMs, suggesting that the
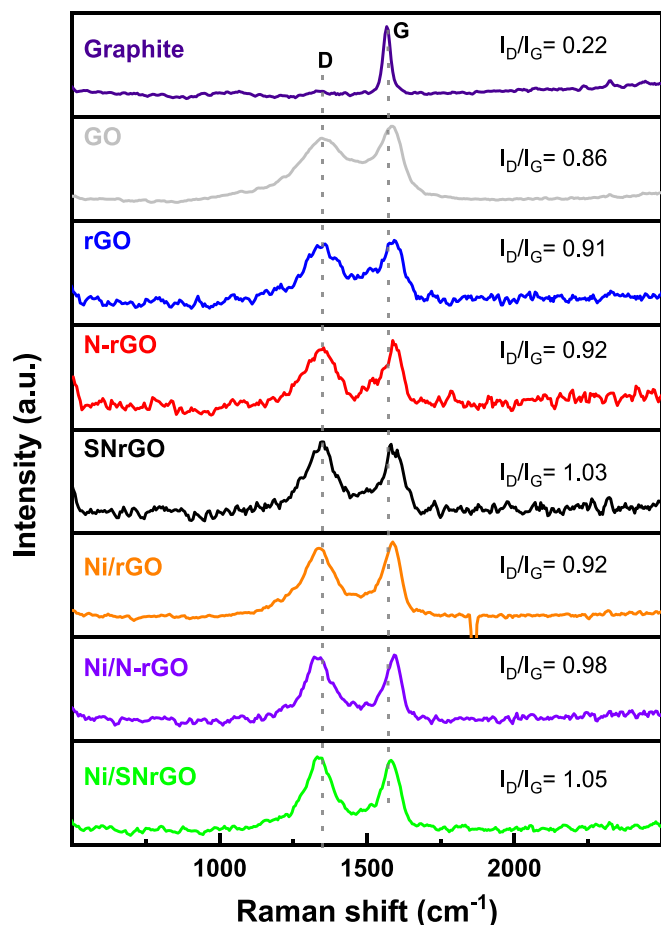
introduction of Ni triggers the increase of the presence of defects in the graphene network.

Finally, XPS analysis of Ni-containing materials was used to provide information on the chemical state of the elements at the catalyst surface. XPS spectra corresponding to the C 1 s, and S 2p core levels for the supporting GMs are reported in a previous work [52]. Briefly, results revealed a high content of oxygen species (C-OH, O—C—O, C=O) in the rGO, confirming that the $Na_3C_6H_5O_7 \cdot 2H_2O$ worked as a weak reducing agent, compared to caffeine and NH_4SCN. In addition, doping with caffeine and NH_4SCN introduces pyridinic, pyrrolic groups and quaternary species [52].

Deconvoluted spectra of the Ni/SNrGO catalyst for C, O, N, S and Ni core levels are depicted in Fig. 3 and data are summarized in Table 1. N 1 s spectrum can be deconvoluted in three main peaks that indicate the presence of different nitrogen species such as pyridinic (398.8 eV) and pyrrolic (400.4 eV) groups and quaternary species (401.1 eV) [21,53–55]. In addition, S 2p spectrum shows two contributions at 162.6 and 163.8 eV, corresponding to S $2p_{3/2}$ and S $2p_{1/2}$, respectively [56]. These two contributions can be attributed to -C—S—C species[57,58].

Ni 2p XPS spectrum presents two contributions at 853.0 and 870.3 eV, corresponding to Ni $2p_{3/2}$ and Ni $2p_{1/2}$, respectively, with two satellite peaks (861.7 and 879.5 eV). The Ni 2p can be deconvoluted into four peaks (Table 1) corresponding to metallic Ni, NiO, Ni(OH)$_2$ and the satellite peak [57,59]. The carbon signal is mostly composed by different oxygenated species (C—O—C, C=O and C-OH), and species associated with the formation of C—C sp^2 (284.6 eV) and C—C sp^3 bonds (285.4 eV) [60]. Generally, C—N/ C—S signals appear at the binding energy of 285.4 eV, making impossible to discern with C—C sp^3 XPS signal.

XPS spectra for Ni/rGO and Ni/*N*-rGO can be seen in the supporting information (Figures S6 and S7). The C 1 s spectrum of Ni/rGO exhibits the characteristic peaks of C—C sp^2 (284.6 eV), C—C sp^3 (285.4 eV) C-OH (286.2 eV), C—O—C (287.8 eV) and C=O (290.5 eV) [21,52,60,61], confirming the presence of epoxide, hydroxyl, and carbonyl groups (Figure S6). The O 1 s spectrum for this catalyst displays a small contribution located at 530.8 eV which can be related to oxidized species of Ni [39]. However, the Ni signal for Ni/rGO does not appear in the survey, even though this metal was detected by XRD and EDX, so it is concluded that Ni is not located at the first nm of the surface. This fact
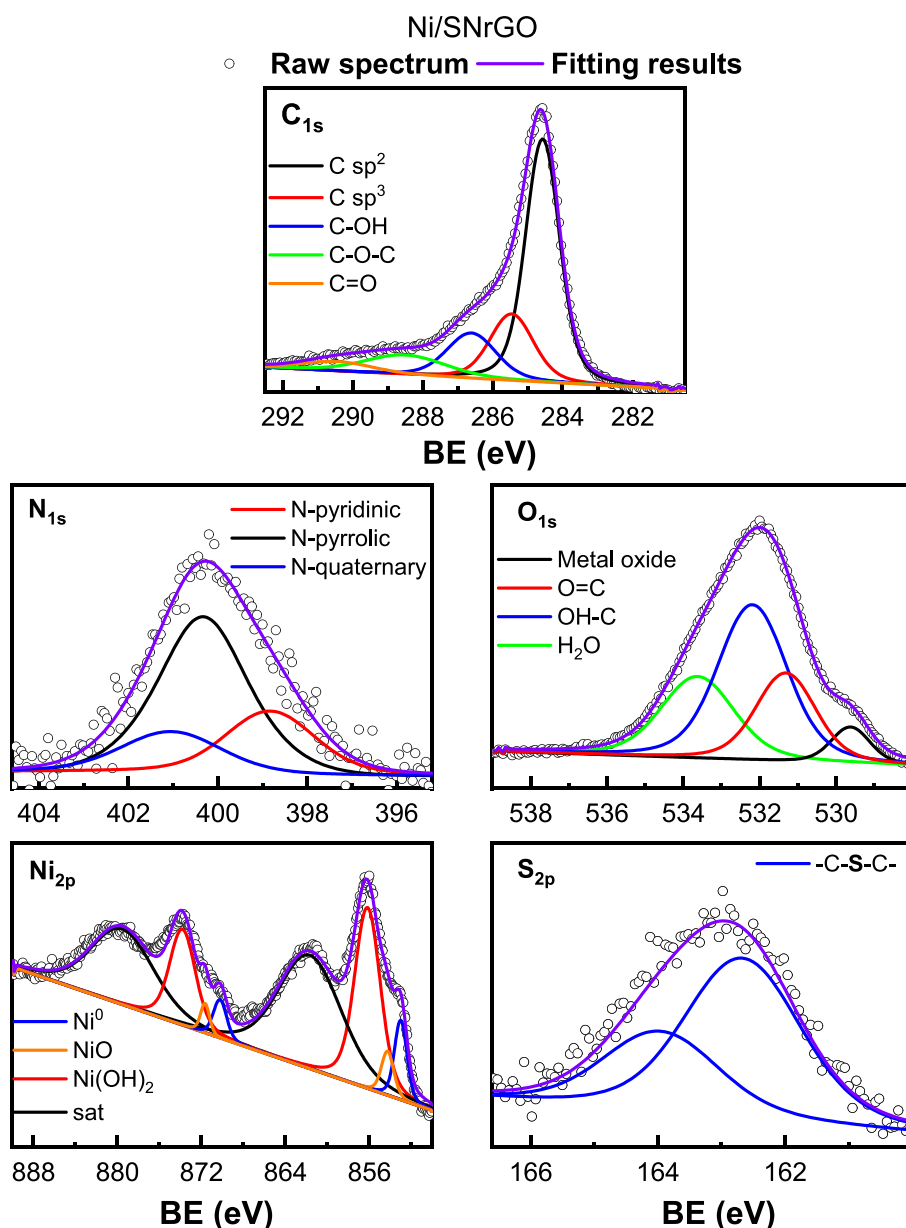

Fig. 3. XPS spectra of Ni/SNrGO.

Table 1
Atomic concentration %, binding energy and assignments of chemical species observed in the surface of Ni-based catalyst by XPS.

Material	Ni/rGO			Ni/*N*-rGO			Ni/SNrGO		
Element	B.E. / eV	Assignment	At. %	B.E. / eV	Assignment	At. %	B.E. / eV	Assignment	At. %
C 1 s	284.6	C sp^2	60.3	284.6	C sp^2	38.0	284.6	C sp^2	52.9
	285.4	C sp^3	5.4	285.4	C sp^3	5.5	285.4	C sp^3	18.4
	286.2	C-OH	24.2	286.7	C-OH	40.5	286.6	C-OH	14.2
	287.8	C—O—C	5.3	288.6	C—O—C	7.4	288.5	C—O—C	10.2
	290.5	C=O	4.8	290.5	C=O	8.6	290.4	C=O	4.3
O 1 s	530.8	Metal oxide	4.4	530.1	Metal oxide	4.5	529.6	Metal oxide	6.1
	532.2	O=C	26.4	531.8	O=C	28.8	531.4	O=C	22.5
	533.5	OH-C	53.5	533.2	OH-C	45.1	532.2	OH-C	46.0
	534.7	H$_2$O	15.8	534.4	H$_2$O	21.6	533.6	H$_2$O	25.4
N 1 s	–	*N*-Pyridinic	–	–	*N*-Pyridinic	–	398.8	*N*-Pyridinic	24.9
	–	*N*-Pyrrolic	–	–	*N*-Pyrrolic	–	400.4	*N*-Pyrrolic	57.2
	–	*N*-Quaternary	–	–	*N*-Quaternary	–	401.1	*N*-Quaternary	17.9
S 2p$_{3/2}$	–	-C—S—C-	–	–	-C—S—C-	–	162.6	-C—S—C-	66.6
S 2p$_{1/2}$	–	-C—S—C-	–	–	-C—S—C-	–	163.8	-C—S—C-	33.4
Ni 2p	–	Ni^0 2p$_{3/2}$	–	852.9	Ni^0 2p$_{3/2}$	2.7	853.0	Ni^0 2p$_{3/2}$	4.7
	–	Ni^0 2p$_{1/2}$	–	870.1	Ni^0 2p$_{1/2}$	1.4	870.3	Ni^0 2p$_{1/2}$	2.4
	–	NiO 2p$_{3/2}$	–	854.3	NiO 2p$_{3/2}$	5.2	854.2	NiO 2p$_{3/2}$	6.6
	–	NiO 2p$_{1/2}$	–	871.8	NiO 2p$_{1/2}$	3.8	871.7	NiO 2p$_{1/2}$	3.8
	–	Ni(OH)$_2$ 2p$_{3/2}$	–	856.2	Ni(OH)$_2$ 2p$_{3/2}$	54.3	856.2	Ni(OH)$_2$ 2p$_{3/2}$	51.5
	–	Ni(OH)$_2$ 2p$_{1/2}$	–	873.8	Ni(OH)$_2$ 2p$_{1/2}$	32.6	873.8	Ni(OH)$_2$ 2p$_{1/2}$	31.0

could be associated with the lower inelastic mean free path of Ni 2p photoelectrons as compared to that of O 1 s photoelectrons.

It should be pointed out, that the survey spectrum of the samples was measured using a pass energy of 15 eV to enhance the intensity of weak peaks. However, no Ni signal was detected in the Ni/rGO sample. For the Ni 2p region (in those samples where Ni is observed, Ni/*N*-rGO and Ni/SNrGO) a lower pass energy of 9 eV was used to enhance the resolution. This improvement in resolution is at the expense of a decrease in intensity, therefore making even more difficult to detect any Ni signal in the Ni/rGO sample. For this reason, the Ni 2p spectrum of Ni/rGO sample was not measured at 9 eV.
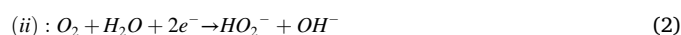
As shown in **Figure S7**, the carbon signal for Ni/*N*-rGO XPS spectrum is mainly composed of different oxygenated species, including epoxide, hydroxyl, and carbonyl groups as in the other Ni-containing materials. The Ni 2p$_{3/2}$ can be deconvoluted in four peaks at 852.9, 854.3, 856.2 and 862.1 eV [62,63], corresponding to Ni(0), NiO, Ni(OH)$_2$ and the satellite peak, respectively. Although N was not detected in Ni/*N*-rGO by XPS, as previously stated, its presence was confirmed by elemental analysis. Considering the noise level for N 1 s signal in the XPS spectra for *N*-rGO (shown in [52]) at 3.8 wt%, it is reasonable that the N 1 s signal would not be reliably detected at the smaller amounts present in Ni/*N*-rGO (1.4 wt%).

XPS analysis (given in Table 1) revealed that Ni/SNrGO is composed by more oxygenated species than its Ni-based catalysts counterparts, which agrees with the results from EDX analysis (see **Table S4**). Moreover, a higher metallic Ni content was observed in Ni/SNrGO sample.

Oxidation is bound to occur when the material is exposed to atmospheric pressure and aqueous media. Thus, Ni(OH)$_2$ detection by XPS can be attributed to the oxidation of the surface of the catalyst, creating a thin layer of Ni(OH)$_2$ mainly localised on the surface [64–67]. The lack of detection of nickel hydroxide by XRD does not directly imply the complete absence in the catalyst, but rather that the Ni(OH)$_2$ phase could be amorphous.

3.1.3. Electrochemical performance towards ORR

The catalytic performance towards the ORR depends on several factors such as geometric and electronic parameters [68–70]. The oxygen reduction reaction in alkaline medium can proceed through two different pathways [71]: (i) the direct four-electron transfer pathway (equation (1) from oxygen to water, and the (ii) two-step (two-electron pathway, eqs. (2) and (3) from oxygen to hydroperoxyl ion (HO$_2^-$).

$$(i): O_2 + 2H_2O + 4e^- \rightarrow 4OH^- \tag{1}$$

$$(ii): O_2 + H_2O + 2e^- \rightarrow HO_2^- + OH^- \tag{2}$$

$$HO_2^- + H_2O + 2e^- \rightarrow 3OH^- \tag{3}$$

In order to study the catalytic activity for the ORR, the RRDE technique was applied (Fig. 4). The top panels show the polarization curves recorded at 2 mV·s^{-1} in 0.1 M NaOH (1600 rpm), meanwhile the bottom ones depict the signal for the peroxide production acquired with the ring electrode at 1.2 V (corresponding to a 2-electron pathway). Hydrogen peroxide percentage (right inset in Fig. 4 **B** and **D**) was calculated using equation (4) [71]. Also, the number of electrons transferred (n$_{electrons}$, Table 2) was calculated (left-upper insets in Fig. 4 **A** and **C**) by the equation (5) [71], where N is the current collection efficiency of the ring (0.22), and j$_D$ and j$_R$ are the ring and disk current densities, respectively. Current densities in Fig. 4 were obtained using the geometric area.

$$\% \ HO_2^- = \frac{200\frac{j_R}{N}}{\left(|j_D| + \frac{j_R}{N}\right)} \tag{4}$$

$$n_{electrons} = \frac{4|j_D|}{\left(|j_D| + \frac{j_R}{N}\right)} \tag{5}$$

The number of transferred electrons with rGO, *N*-rGO and SNrGO as electrocatalysts were 3.6, 3.6 and 3.7, respectively. Once Ni was deposited on the supporting materials, the number of transferred electrons increased, showing values of 3.6, 3.7 and 3.9 for Ni/rGO, Ni/*N*-rGO and Ni/SNrGO, respectively, at potentials below 0.8 V$_{RHE}$. Therefore, Ni deposition leads to favour the 4-electron pathway for the oxygen reduction reaction in these materials.

To compare the different catalysts' performance for ORR, the data has been summarised in Table 2. The kinetic parameters obtained from the polarization curves (Fig. 4), as well as the current density at two fixed potentials and the achieved potential at -1 mA·cm^{-2} have been included.

ORR results revealed that the insertion of N into the graphenic network increased the E$_{onset}$ towards the ORR, while the dual S/N-doping enhanced the electron transfer and achieved higher current density at 0.6 V$_{RHE}$ (-1.56 mA·cm^{-2}). Nickel deposition led to lower overpotentials compared to the supporting GMs. Ni/SNrGO developed a higher E$_{onset}$ (0.84 V) than the other electrocatalysts with Ni NPs, which indicates that the ORR occurs more easily on the surface of this
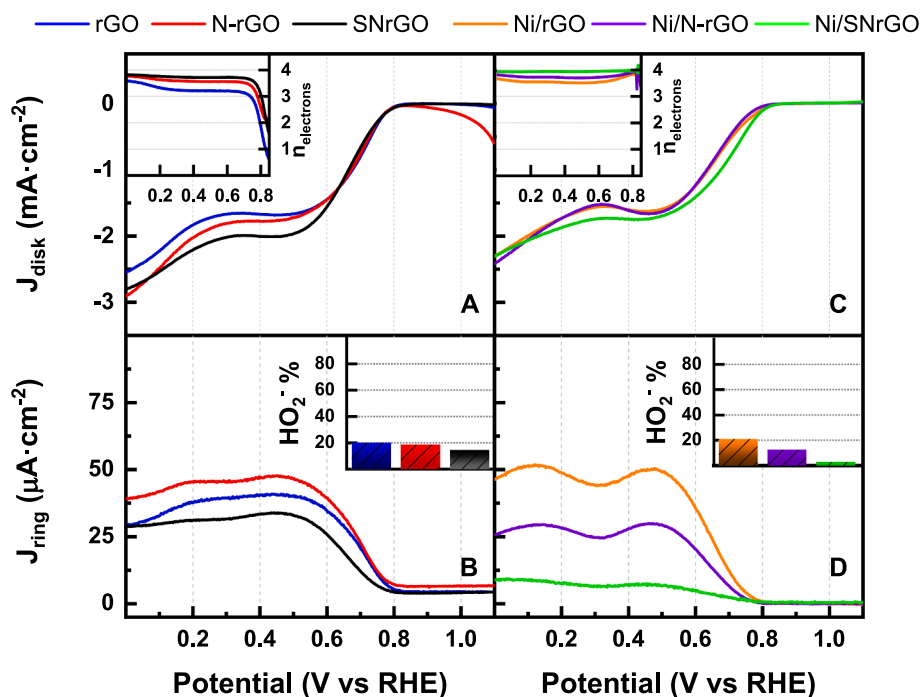
Fig. 4. LSV curves for ORR recorded in O_2-saturated at 1600 rpm in 0.1 M NaOH at 2 mV·s^{-1} for the GMs (A) and Ni-based catalysts (C) (top panels); current densities developed at 1.2 V at the Pt ring electrode for GMs (C) and Ni electrocatalysts (D) (bottom panels). Number of electrons (inset, left of A and C) and as percentage of HO_2^- production at the Pt ring (inset, right of B and D).

Table 2
Kinetic parameters for ORR at the electrodes in O_2– saturated 0.1 M NaOH.

Catalyst	J^a (mA/cm^2)	J^b (mA/cm^2)	E^c (V)	E_{onset} (V)	Tafel Slope^d (mV/dec)	Tafel Slope^e (mV/dec)	HO_2^{-f} (%)	$E_{1/2}$ (V)
rGO	−1.45	−0.32	0.67	0.79	55	103	20.2	0.63
N-rGO	−1.45	−0.29	0.67	0.78	67	101	20.8	0.60
SNrGO	−1.56	−0.27	0.67	0.78	65	111	13.3	0.62
Ni/rGO	−1.24	−0.27	0.64	0.83	56	126	22.8	0.66
Ni/*N*-rGO	−1.23	−0.20	0.63	0.81	53	106	13.7	0.65
Ni/SNrGO	−1.41	−0.43	0.68	0.84	48	118	3.1	0.69

a: at 0.6 V; **b:** at 0.75 V; **c:** at −1 mA·cm^{-2}; **d:** low overpotential and **e:** high overpotential regions.

electrode. Ni-based catalysts develop the best performance towards this reaction in terms of onset potential values. Furthermore, a 4-electron pathway reduction of oxygen occurred when doping with S and N (SNrGO and Ni/SNrGO).

The order for hydrogen peroxide production (%) decreases for the Ni containing materials as follows: Ni/rGO > Ni/*N*-rGO ≫ Ni/SNrGO (see Table 2). Results obtained for the different supporting materials, as well as the rGO, are similar to those reported in previous works [5,58]. Although in the case of Ni/rGO the HO_2^- production slightly increases, in the case of doped-graphene materials drastically diminishes, especially in the case of the bi-doped material from 14.6 to 3.0 %.

Similar current densities were achieved for all electrocatalysts, falling, all of them, within a range between −1.2 and −1.6 mA·cm^{-2}. Although these values are quite low, it was observed that the 4-electron pathway is favoured for S and *N*-doped catalysts (SNrGO and Ni/SNrGO), as the percentage of hydrogen peroxide production decreased significantly. It is worth mentioning the value obtained for Ni/SNrGO, as it produced ca. five times less HO_2^- (3.0 %) than its supporting material (14.6 %).

Half-wave potential ($E_{1/2}$), defined as the potential to reach half of the limiting current density obtained from the LSV curve, is commonly used to evaluate the oxygen reduction reaction's performance. Certainly, the lower the difference between the $E_{1/2}$ and the

thermodynamic potential value (1.23 vs RHE), the better the catalytic response of the material towards the ORR [58,72,73]. Although the determination of the half-wave potential has a relatively large error due to the absence of a well-defined plateau, some conclusions can be attained from the values in Table 2. Ni-based catalysts exhibited higher $E_{1/2}$ values, suggesting that Ni deposition leads to better ORR performance. For instance, Ni/SNrGO displayed the highest half-wave potential value of all catalysts studied (0.69 V_{RHE}).

As previously introduced, Ni deposition commonly leads to an enhancement of electrocatalytic activity towards the oxygen reduction reaction. Nevertheless, the limiting current observed for the Ni-based electrocatalysts in Fig. 4 was slightly lower than their GM counterparts. For better understanding of these results, LSV curves were normalized with the electrochemical active surface area (ECSA). RRDE theory [71,74] applies to planar electrodes but in the present paper, the configuration of the working electrode is different and consists of a thin, porous layer of the catalysts fixed on a planar disk. Moreover, Ni content is different in the catalysts. So, referring to ECSA, both parameters, which influences the electrochemical activity of the materials, are considered. The calculations regarding the ECSA are detailed in the supporting information **Figures S8-S10**), with the results depicted in **Figure S10** being used alongside the data from Fig. 4, to obtain the curves shown in Fig. 5. It is noted that, as shown in **Figure S10**, the
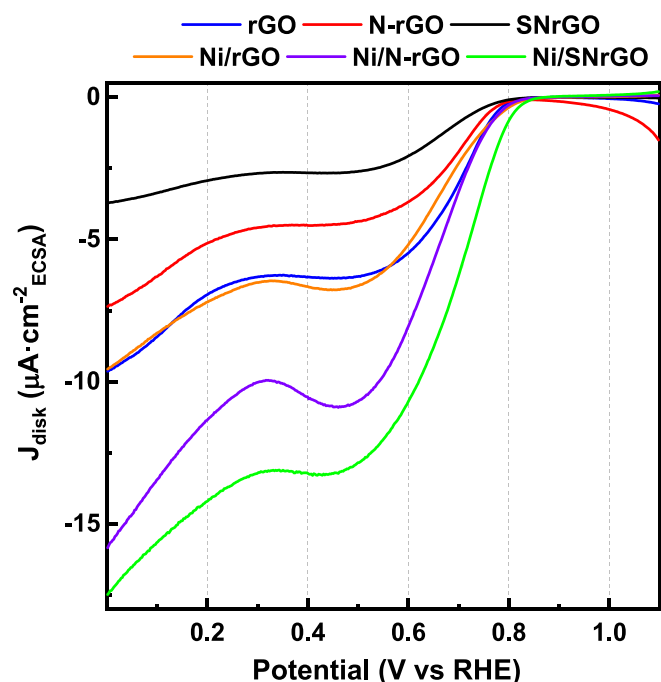
Fig. 5. LSV normalized with electrochemical surface area (ECSA) of the materials.

Fig. 6. Tafel plots obtained from the ORR polarization curves in Figs. 4 and 5 in NaOH 0.1 M at 1600 rpm and 2 mV·s^{-1}.

deposition of Ni implies an overall decrease in electrochemical active surface area values with a significant drop in the materials with heteroatoms (Ni/*N*-rGO and Ni/SNrGO) [75]. This drop justifies the decrease in the current densities observed in Fig. 4.

Considering Fig. 5, the LSV obtained for rGO and Ni/rGO are quite similar in terms of limiting current, while the curves corresponding to Ni/*N*-rGO and Ni/SNrGO exhibit a higher limiting current value. These curves prove that Ni deposition enhances the catalytic activity, leading to a four-electron pathway towards the ORR and higher onset potential values.

According to the previous values, it can be established that the catalytic activity towards the ORR increases in the following order: Ni/rGO < Ni/*N*-rGO < Ni/SNrGO in terms of ORR onset potential, current density at a fixed potential, number of electrons exchanged and percentage of HO$_2^-$ produced during the reaction.

Tafel plots at low overpotentials (~0.8 V) and high overpotentials (~0.7 V) were used for the study of the ORR mechanism at these materials (Fig. 6). These values are frequently used to determine the rate-determining step (RDS). In alkaline medium, the operating mechanisms accepted for the ORR for these materials is the associative one [69]:

$$O_2 \rightarrow O_{2(ads)} \tag{6}$$

$$O_{2(ads)} + H_2O + e^- \rightarrow OOH_{(ads)} + OH^- \tag{7}$$

$$OOH_{(ads)} + e^- \rightarrow O_{(ads)} + OH^- \tag{8}$$

$$O_{(ads)} + H_2O + e^- \rightarrow OH_{(ads)} + OH^- \tag{9}$$

$$OH_{(ads)} + e^- \rightarrow OH^- \tag{10}$$

The Tafel slopes for all the materials studied are depicted in Fig. 6 and summarised in Table 2. At low overpotentials, which is the kinetic-diffusion controlled region, the GMs exhibit a Tafel slope close to 60 mV·dec^{-1}. The RDS for this value is considered to be a chemical step after an electrochemical step [3,69,76–78]. Therefore, the following chemical step (eq. (7.1) has been proposed in [58] for the aforementioned mechanism.
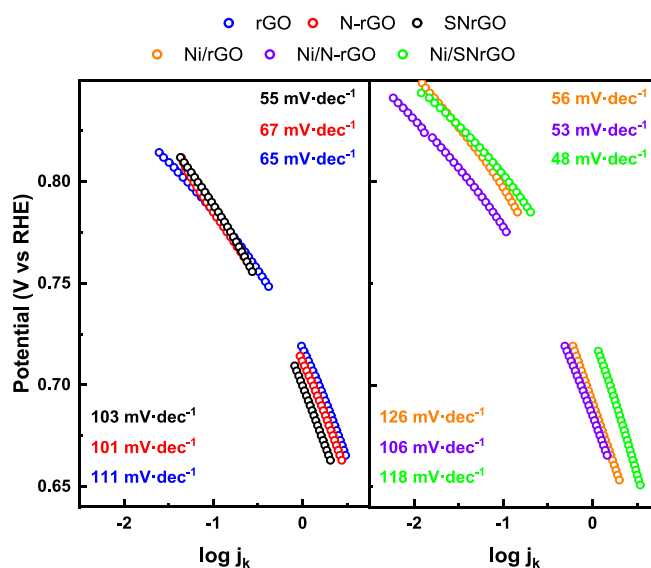
$$OOH_{(ads)} \rightarrow O_{(ads)} + OH_{(ads)} \tag{7.1}$$

In the same potential region, Ni deposition led to a decrease in the Tafel slope values for the doped materials. For instance, for Ni/SNrGO a Tafel slope value closer to 40 mV·dec^{-1} was obtained. This value is related to a second electrochemical step as RDS (eq. (8), suggesting a change in the mechanism [78].

Tafel slope values for the supporting GMs are in agreement with our previous works [5,58]. Hao et al. [79] have reported Tafel slope values of 48.2 and 47.8 mV·dec^{-1} at low overpotentials for Ni$_x$Co$_y$O$_4$/Co–NC (Co/N decorated graphene composite) and Ni$_x$Co$_y$O$_4$/Co–NG (nitrogen decorated graphene), respectively. On the other hand, Al-Enizi et al. [25] reported higher Tafel slope values for their Cu-Ni@rGO nanocomposite (~78 mV·dec^{-1}). Thus, Tafel slope values for Ni-based catalysts in this work agree with the literature.

At high overpotentials, Tafel slope varies between 101 and 111 mV·dec^{-1} for GMs and between 106 and 126 mV·dec^{-1} for Ni catalysts (Fig. 6). A Tafel slope of 120 mV·dec^{-1} suggests that the RDS is related to the first electrochemical step (eq. (7), involving the first single electron transfer [77]. Therefore, a clear influence of the potential over the mechanism of ORR can be discerned, as commonly described occurrence for this reaction [5,58]. Nevertheless, it should be noted that the presence of hydrogen peroxide may increase these values, as stated by Schmidt et al. [80], blocking the active sites for the ORR.

3.1.4. Preliminary studies of stability in alkaline fuel cell for ORR

Stability test preliminary studies towards oxygen reduction reaction (Figure S11) revealed that supporting materials exhibit a faster cell voltage decay and higher performance loss than their Ni-based catalyst counterparts. Certainly, oscillations were observed for the supporting materials. These oscillations are associated with current drops, which occur when the potential reaches values close to 0.3 V to prevent a possible shutdown of fuel cell equipment. The materials with continuous changes in current load are then more unstable, as degradation of the electrode occurs. The performance loss for Ni containing catalysts increases as follows: Ni/SNrGO ≪ Ni/rGO < Ni/*N*-rGO, that is, Ni/SNrGO is the most stable materials under fuel cell conditions. Those electrocatalysts that had the forementioned current drops (rGO, *N*-rGO and SNrGO) had their performance loss values softened (26.8, 23.6 and 4.2 %, respectively), thus skewing the absolute results. It is implied then

that, had these safety changes not occurred, the values would be much higher.

Generally, it could be stated that Ni deposition improves the stability of the materials. Nonetheless, the electrochemical response in an alkaline fuel cell and their stability using these catalysts as cathodes for the ORR reaction would be the main topic of an upcoming publication.

3.2. Electrochemical performance towards HER

Polarization curves at 2 mV·s^{-1} were carried out to establish the catalytic activity towards the hydrogen evolution reaction (Fig. 7) in H$_2$-saturated 1 M NaOH. These curves show a qualitative trend where all the supporting GMs displayed poor HER activity. Nevertheless, it is clearly enhanced in the Ni-based materials compared to the supports. The deposition of Ni vastly shifts the reaction towards more positive values and, therefore, towards lower overpotentials (Table 3). While rGO revealed poor HER activity, Ni/*N*-rGO, remarkably, developed the best performance among the different materials with an onset potential of −210 mV$_{RHE}$.

Current densities at two fixed potentials are depicted in Fig. 8 to ease the comparison between the different catalysts' performances for HER. Furthermore, representative electrochemical parameters are given in Table 3. Ni/*N*-rGO displays the best catalytic efficiency reaching −33.74 mA·cm^{-2} at −0.35 V$_{RHE}$, followed by Ni/rGO with −13.55 mA·cm^{-2}, whereas Ni/SNrGO only achieved −9.49 mA·cm^{-2}.

For the supporting materials at −0.8 V$_{RHE}$ (more negative potentials are needed to achieve significative current density values). At −0.8 V$_{RHE}$ (Fig. 8), rGO reached −24.86 mA·cm^{-2}, followed by *N*-rGO with −57.95 mA·cm^{-2} and SNrGO with −15.94 mA·cm^{-2}, following the same trend previously described for Ni-catalysts and concluding that the graphene support is conditioning the final performance of the material towards the HER (Fig. 8). Accordingly, at a fixed current density of −10 mA·cm^{-2} (Table 3), the performance based on the potential achieved follows the subsequent order: SNrGO < rGO < *N*-rGO < Ni/SNrGO < Ni/
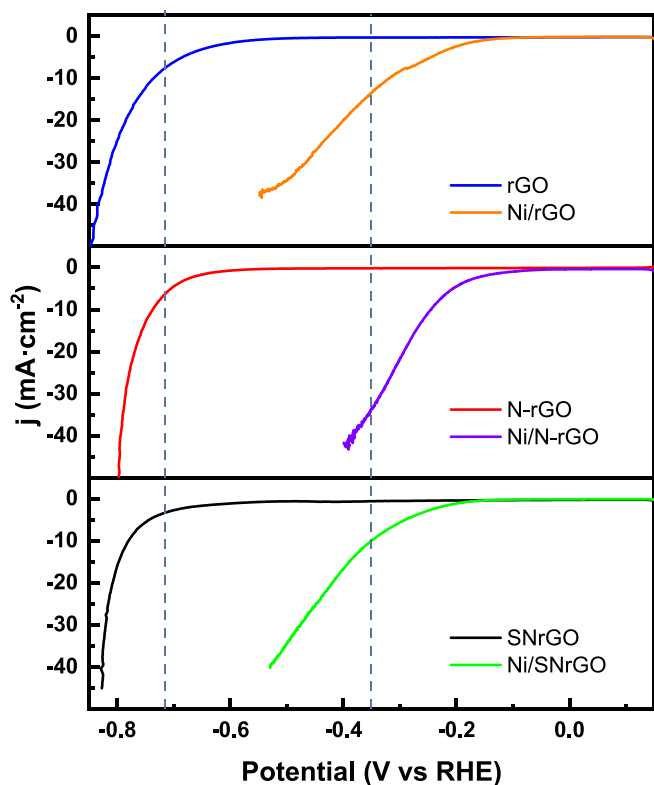

Fig. 7. Polarization curves for all the electrocatalysts towards HER in NaOH 1 M recorded at 2 mV·s^{-1} and 1600 rpm.

Table 3
Electrochemical parameters for HER on the different catalysts.

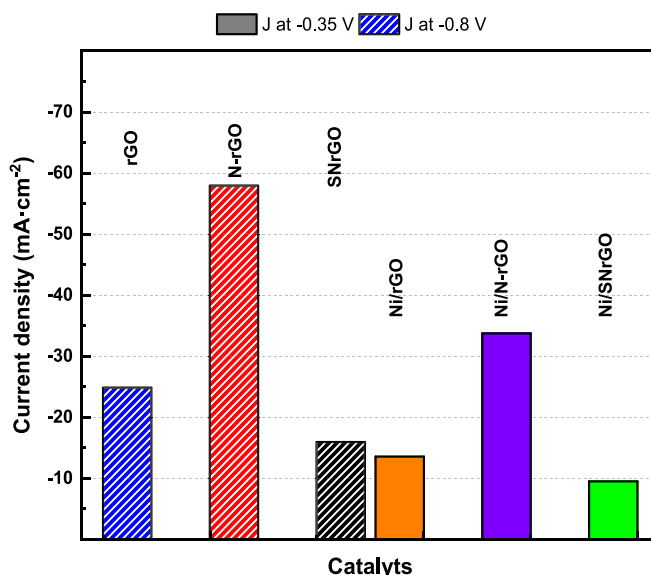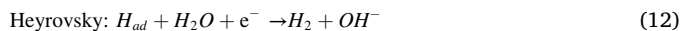| Catalyst	E$_{onset}$ (V)	E^a(V)	Tafel slope (mV·dec^{-1})
rGO	−0.76	−0.74	162
N-rGO	−0.74	−0.73	111
SNrGO	−0.78	−0.78	123
Ni/rGO	−0.23	−0.32	137
Ni/*N*-rGO	−0.21	−0.25	129
Ni/SNrGO	−0.28	−0.35	147

a: current density was fixed at −10 mA·cm^{-2}.

Fig. 8. Bar graph displaying the current density (J) at −0.35 V$_{RHE}$ for the Ni-based catalysts and at −0.8 V$_{RHE}$ for the supporting GMs towards HER.

rGO < Ni/*N*-rGO. The supporting materials and their Ni-based catalysts are again visibly distinguished, with Ni/*N*-rGO achieving the best potential value (-250 mV vs RHE). The results demonstrate that doping graphene with N and the presence of Ni nanoparticles enhance the HER, producing lower overpotentials and higher current densities.

As in the case of the ORR, Tafel slopes were also estimated to establish the RDS of the HER. In alkaline medium, the hydrogen evolution reaction follows the following pathways [78,81]:

Volmer: $H_2O + e^- \rightarrow H_{ad} + OH^-$ (11)

Heyrovsky: $H_{ad} + H_2O + e^- \rightarrow H_2 + OH^-$ (12)

Tafel: $H_{ad} + H_{ad} \rightarrow H_2$ (13)

The theoretical Tafel slopes for HER are 120, 40 and 30 mV·dec^{-1}, corresponding to Volmer (eq. (11)), Heyrovsky (eq. (12)) and Tafel (eq. (13)), respectively. The first step (Volmer) is also called discharge reaction, in which an electrochemical adsorption of hydrogen occurs. Afterwards, the reaction could take place in two different pathways: i) an electrochemical water-mediated desorption of hydrogen (Heyrovsky step); or ii) the chemical desorption (Tafel)[81]. In this work, Tafel slopes for all the materials were obtained from HER polarization curves and the values can be seen in Fig. 9.

For all materials, the Tafel slopes are around 120 mV/dec which indicates that the RDS would be the Volmer step. Thus, it seems that the addition of Ni does not produce a change in the mechanism but an increase in the activity with changes in the onset potential and current densities. However, it is remarkable that in most cases Tafel slope values are much higher than 120 mV/dec. Thus, rGO develops the highest Tafel slope of 162 mV/dec and for Ni/SNrGO 147 mV/dec. These deviations
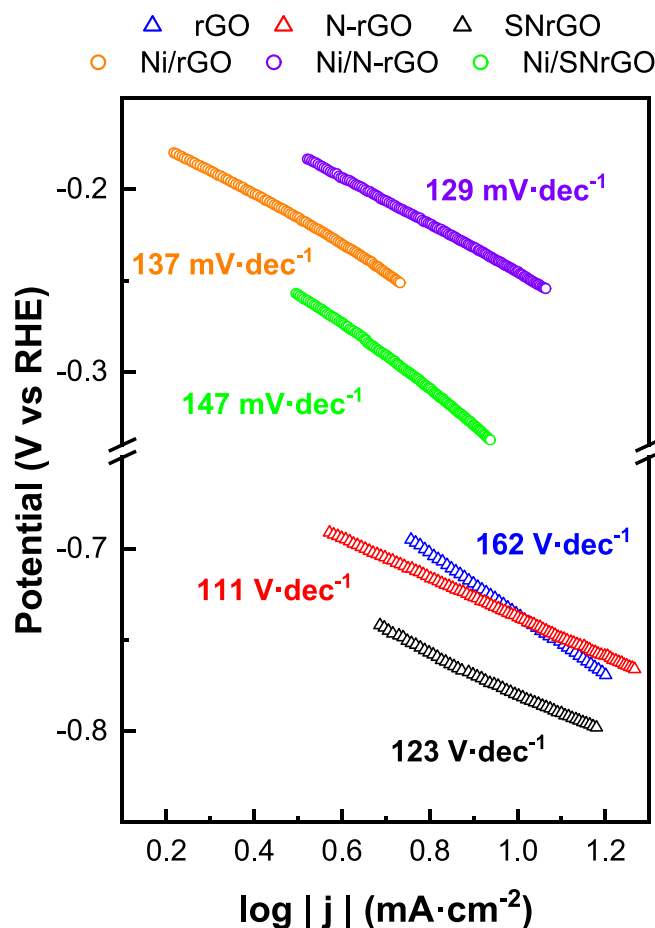
Fig. 9. HER Tafel slopes for all the materials studied.

Fig. 10. Bode representations for a-c) supporting materials (GMs) and d-f) Ni-based catalysts at -10 mA·cm^2 in 0.1 M NaOH.

from theoretical values are most likely due to the contribution of reduction currents of surface oxide species which take place in the same potential region, as Ni oxides identified in XPS and XRD analysis (Table 1 and Fig. 1, respectively). This effect has already been described in the literature [9,29,82]. Thus, for accurate determination of the onset potential and Tafel slopes and further discussion of the mechanism, a differential electrochemical mass spectrometry (DEMS) study is required [29,78].

Finally, electrochemical impedance spectroscopy (EIS) measurements were performed at the potential achieved at -10 mA·cm^{-2} for each catalyst over a wide range of frequencies (100 kHz to 0.1 Hz) in a 0.1 M NaOH solution to further investigate the kinetics on the hydrogen evolution reaction. Results are depicted in **Figure S12** (Nyquist plots) and Fig. 10 (Bode graphs).

The impedance data for the HER on GMs reveals that rGO and *N*-rGO displayed a capacitive semicircle, followed by an increase in the resistance, attributed to Warburg diffusion. According to the literature [83–86], Warburg diffusion is easily identified as a straight line with a slope of 45 degrees, usually at higher frequencies (**Figure S12**, left). The block-diffusion Warburg is commonly attributed to diffusion of electroactive species in the electrode [84], which fits the plots of both rGO and *N*-rGO. Interestingly, SNrGO does not exhibit the same diffusion pattern as the forementioned supporting materials, but follows the shape of a semicircle, attributed to a charge-transfer resistance. Then, it can be stated that the dual S—N doping has a synergetic effect leading to lower resistances. Regarding the Ni-based materials, their plots (**Figure S12**, right) also follow a semicircle which are associated with the hydrogen evolution reaction. Nonetheless, the radius for these materials is drastically smaller, that is, the charge-transfer resistance is smaller, indicating an improvement over HER kinetics and electron transfer.
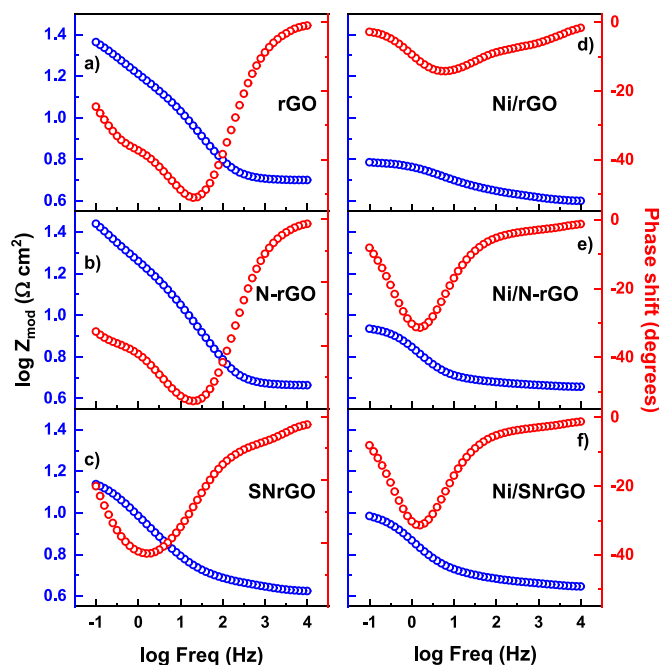
Two curves for each material are given in the Bode plots (Fig. 10). The blue one corresponds to log Z_{mod} vs log frequency associated with the charge-transfer resistance, and the red one corresponds to the phase shift vs log frequency related to the electron transfer. It is observed that Ni deposition leads to overall lower Z_{mod} values thus improving HER kinetics. On the other hand, heteroatom doping increases the charge-transfer resistance.

Ni/rGO was found to be the most active catalyst towards the HER, according to **Figure S12** and Fig. 10, as it exhibited lower charge-transfer resistance values (log Z_{mod}) and better electron transfer (at higher frequency values). Therefore, since there is a discrepancy between results from **Figures 10** and **S12** and Figs. 7-9, exact determination of kinetic parameters and mechanism using differential electrochemical mass spectrometry (DEMS) study becomes necessary, as previously indicated, and would be the main topic of a forthcoming publication.

4. Conclusions

In the present work, low-cost catalysts containing Ni NPs supported on graphene-based materials were successfully synthesised by the borohydride method. Physicochemical characterisation was used to establish the surface composition and confirms the good distribution of Ni NPs on the different graphene catalysts. The catalytic activity towards the ORR and HER has been studied in alkaline medium, establishing the role of graphene doping on the performances obtained.

Results for the ORR revealed that supporting Ni on graphene materials leads to lower overpotentials for the reaction and a decrease in the amount of hydrogen peroxide produced compared to bare GMs. However, the enhancement is not substantial. It is observed that S/N dual doping enhances the catalytic activity towards the 4-electron pathway. In terms of stability, depositing Ni has shown to have an overall positive effect, making these catalysts more resilient to degradation than its GM counterparts. Notably, the electrocatalyst doped with S and N demonstrated to be the most stable one. Kinetic parameters indicate that Ni/SNrGO, that is, the Ni-based catalyst supported on the graphene material doped with both S and N, develops the best performance from all studied catalysts for the ORR in alkaline medium, demonstrating the remarkable

effect of doping with heteroatoms. However, the efficiency of these materials is poor compared to other catalysts in the literature.

In contrast, an outstanding enhancement of the catalytic activity of the graphene materials towards the HER was observed after the addition of Ni NPs, leading to lower overpotentials and higher current densities for the reaction. In this case, the best performance was achieved by the materials doped with N, with Ni/*N*-rGO displaying the most remarkable results (E$_{onset}$: −0.21 V$_{RHE}$). Opposite to the ORR, the presence of S in the catalyst produces a decrease in the activity regarding the HER. Ni/rGO was found to be the most active catalyst towards the hydrogen evolution reaction, according to EIS results, exhibiting lower charge-transfer resistance values.

Based on these results, it is proved that N and N/S doped GMs influence the activity of Ni-based catalysts for both ORR and HER. It would be interesting, therefore, to carry out studies of the electrochemical response in an alkaline fuel cell and their stability using these materials as cathodes for the ORR reaction. And, on the other hand, to achieve a deep understanding of the HER mechanism, the exact determination of the kinetic parameters could be carried out by applying DEMS. Both studies will be the purpose of future research.

CRediT authorship contribution statement

Declaration of competing interest

The authors declare that they have no known competing financial interests or personal relationships that could have appeared to influence the work reported in this paper.

Data availability

Data will be made available on request.

Acknowledgements

Appendix A. Supplementary data

Supplementary data to this article can be found online at https://doi.org/10.1016/j.ica.2024.122008.

References

[1] Z. Qi. Proton exchange membrane fuel cells, CRC Press, 2013, https://doi.org/10.1201/b15499.

[2] M. del Cueto, P. Ocón, J.M.L. Poyato, Comparative study of oxygen reduction reaction mechanism on nitrogen-, phosphorus-, and boron-doped graphene Surfaces for fuel cell applications, J. Phys. Chem. C. 119 (2015) 2004–2009, https://doi.org/10.1021/jp512588r.

[3] L. Yu, X. Pan, X. Cao, P. Hu, X. Bao, Oxygen reduction reaction mechanism on nitrogen-doped graphene: a density functional theory study, J. Catal. 282 (2011) 183–190, https://doi.org/10.1016/j.jcat.2011.06.015.

[4] S. Sui, X. Wang, X. Zhou, Y. Su, S. Riffat, C. Jun Liu, A comprehensive review of pt electrocatalysts for the oxygen reduction reaction: nanostructure, activity, mechanism and carbon support in PEM fuel cells, J. Mater. Chem. A. 5 (2017) 1808–1825, https://doi.org/10.1039/C6TA08580F.

[5] L.M. Rivera, S. Fajardo, M. del C. Arévalo, G. García, E. Pastor, S-and N-doped graphene nanomaterials for the oxygen reduction reaction, Catalysts. 7 (2017), https://doi.org/10.3390/catal7090278.

[6] A. Lasia, ScienceDirect mechanism and kinetics of the hydrogen evolution reaction, Int. J. Hydrogen Energy. 44 (2019) 19484–19518, https://doi.org/10.1016/j.ijhydene.2019.05.183.

[7] H. Wang, L. Gao, Recent developments in electrochemical hydrogen evolution reaction, Curr. Opin. Electrochem. 7 (2018) 7–14, https://doi.org/10.1016/j.coelec.2017.10.001.

[8] M. Nemiwal, T.C. Zhang, D. Kumar, Graphene-based electrocatalysts: hydrogen evolution reactions and overall water splitting, Int. J. Hydrogen Energy. 46 (2021) 21401–21418, https://doi.org/10.1016/j.ijhydene.2021.04.008.

[9] S. Díaz-coello, J.A. Palenzuela, M.M. Afonso, E. Pastor, G. García (Eds.), WC modi fi ed with ionic liquids for the hydrogen evolution reaction in alkaline solution, 2021, p. 880, https://doi.org/10.1016/j.jelechem.2020.114878.

[10] E. Riva Sanseverino, L.Q. Luu, Critical raw materials and supply chain disruption in the energy transition, Energies. 15 (2022) 5992, https://doi.org/10.3390/en15165992.

[11] R. Stropnik, A. Lotrič, A. Bernad Montenegro, M. Sekavčnik, M. Mori, Critical materials in PEMFC systems and a LCA analysis for the potential reduction of environmental impacts with EoL strategies, Energy Sci. Eng. 7 (2019) 2519–2539, https://doi.org/10.1002/ese3.441.

[12] Y. Chen, Z. Ren, H. Fu, X. Zhang, G. Tian, H. Fu, NiSe-Ni0.85Se heterostructure nanoflake arrays on Carbon paper as efficient electrocatalysts for overall water splitting, Small. 14 (2018) 1–10, https://doi.org/10.1002/smll.201800763.

[13] S. Sarner, A. Schreiber, N.H. Menzler, O. Guillon, Recycling strategies for solid oxide cells, Adv. Energy Mater. 2201805 (2022), https://doi.org/10.1002/aenm.202201805.

[14] H.A. Miller, Green hydrogen from anion exchange membrane water electrolysis, Curr. Opin. Electrochem. 36 (2022) 101122, https://doi.org/10.1016/j.coelec.2022.101122.

[15] C. Santoro, A. Lavacchi, P. Mustarelli, V. Di Noto, L. Elbaz, D.R. Dekel, F. Jaouen, What is next in anion-exchange membrane water electrolyzers? bottlenecks, benefits, and future, ChemSusChem 15 (2022), https://doi.org/10.1002/cssc.202200027.

[16] L.M. Salonen, D.Y. Petrovykh, Y.V. Kolen'ko, Sustainable catalysts for water electrolysis: selected strategies for reduction and replacement of platinum-group metals, Mater. Today Sustain. 11–12 (2021) 100060, https://doi.org/10.1016/j.mtsust.2021.100060.

[17] A.K. Giri, Oxygen reduction reaction in hydrogen fuel cells, Elsevier Inc., 2022, https://doi.org/10.1016/B978-0-323-88508-9.00009-4.

[18] A. Lavacchi, H. Miller, F. Vizza. Nanotechnology in electrocatalysis for energy, Springer, New York, New York, NY, 2013, https://doi.org/10.1007/978-1-4899-8059-5.

[19] L.T. Soo, K.S. Loh, A.B. Mohamad, W.R.W. Daud, W.Y. Wong, Effect of nitrogen precursors on the electrochemical performance of nitrogen-doped reduced graphene oxide towards oxygen reduction reaction, J. Alloys Compd. 677 (2016) 112–120, https://doi.org/10.1016/j.jallcom.2016.03.214.

[20] D. Chanda, A.S. Dobrota, J. Hnát, Z. Sofer, I.A. Pašti, N.V. Skorodumova, M. Paidar, K. Bouzek, Investigation of electrocatalytic activity on a N-doped reduced graphene oxide surface for the oxygen reduction reaction in an alkaline medium, Int. J. Hydrogen Energy. 43 (2018) 12129–12139, https://doi.org/10.1016/j.ijhydene.2018.05.012.

[21] G. Periyasamy, K. Annamalai, I.M. Patil, B. Kakade, Sulfur and nitrogen co-doped rGO sheets as efficient electrocatalyst for oxygen reduction reaction in alkaline medium, Diam. Relat. Mater. 114 (2021) 108338, https://doi.org/10.1016/j.diamond.2021.108338.

[22] R. Sibul, E. Kibena-Põldsepp, U. Mäeorg, M. Merisalu, A. Kikas, V. Kisand, A. Treshchalov, V. Sammelselg, K. Tammeveski, Sulphur and nitrogen co-doped graphene-based electrocatalysts for oxygen reduction reaction in alkaline medium, Electrochem. Commun. 109 (2019) 106603, https://doi.org/10.1016/j.elecom.2019.106603.

[23] L.M. Rivera, G. García, E. Pastor, Novel graphene materials for the oxygen reduction reaction, Curr. Opin. Electrochem. 9 (2018) 233–239, https://doi.org/10.1016/j.coelec.2018.05.009.

[24] M. Luis-Sunga, S.J. Martínez, J.L. Rodríguez, G. García, E. Pastor, Graphene-based materials as highly promising catalysts for energy storage and conversion applications, Nanostructured Multifunct. Mater. Synth. Charact. Appl. Comput. Simul. (2021) 230–260, https://doi.org/10.1201/9780367822194-11.

[25] A.M. Al-Enizi, M. Ubaidullah, J. Ahmed, H. Alrobei, S.M. Alshehri, Copper nickel@ reduced graphene oxide nanocomposite as bifunctional electro-catalyst for excellent oxygen evolution and oxygen reduction reactions, Mater. Lett. 260 (2020) 126969, https://doi.org/10.1016/j.matlet.2019.126969.

[26] S. Samad, K.S. Loh, W.Y. Wong, W. Sudarsono, T.K. Lee, W.R. Wan Daud, Effect of various Fe/Co ratios and annealing temperatures on a Fe/Co catalyst supported with nitrogen-doped reduced graphene oxide towards the oxygen reduction reaction, J. Alloys Compd. 816 (2020) 152573, https://doi.org/10.1016/j.jallcom.2019.152573.

[27] M.M. Dinesh, D. Liang, H. Zhang, X. Ma, X. Zhou, T. Huang, S. Mao, J. Mao, Catalytic performances of NiCuP@rGO and NiCuN@rGO for oxygen reduction and oxygen evolution reactions in alkaline electrolyte, ChemistrySelect. 5 (2020) 5855–5863, https://doi.org/10.1002/slct.202001001.

[28] H. Zhang, H. Li, H. Wang, K. He, S. Wang, Y. Tang, J. Chen, NiCo2O4/N-doped graphene as an advanced electrocatalyst for oxygen reduction reaction, J. Power Sources. 280 (2015) 640–648, https://doi.org/10.1016/j.jpowsour.2015.01.147.

[29] A. Bazan-Aguilar, G. García, E. Pastor, J.L. Rodríguez, A.M. Baena-Moncada, In-situ spectroelectrochemical study of highly active ni-based foam electrocatalysts for hydrogen evolution reaction, Appl. Catal. B Environ. 336 (2023) 122930, https://doi.org/10.1016/j.apcatb.2023.122930.

[30] M.L.N. Thi, T.H. Tran, P.D. Hai Anh, H.-T. Nhac-Vu, Q.B. Bui, Hierarchical zinc–nickel phosphides nanosheets on 3D nickel foam as self-support electrocatalysts for hydrogen evolution reaction, Polyhedron. 168 (2019) 80–87, https://doi.org/10.1016/j.poly.2019.04.050.

[31] Z. Yin, F. Chen, A facile electrochemical fabrication of hierarchically structured nickel-copper composite electrodes on nickel foam for hydrogen evolution reaction, J. Power Sources. 265 (2014) 273–281, https://doi.org/10.1016/j.jpowsour.2014.04.123.

[32] X. Zhang, Y. Li, Y. Guo, A. Hu, M. Li, T. Hang, H. Ling, 3D hierarchical nanostructured Ni–Co alloy electrodes on porous nickel for hydrogen evolution reaction, Int. J. Hydrogen Energy. 44 (2019) 29946–29955, https://doi.org/10.1016/j.ijhydene.2019.09.193.

[33] Z.Z. Liu, X. Shang, B. Dong, Y.M. Chai, Triple Ni-Co-Mo metal sulfides with one-dimensional and hierarchical nanostructures towards highly efficient hydrogen evolution reaction, J. Catal. 361 (2018) 204–213, https://doi.org/10.1016/j.jcat.2018.03.004.

[34] E.A. Franceschini, G.I. Lacconi, Synthesis and Performance of Nickel/Reduced Graphene Oxide Hybrid for Hydrogen Evolution Reaction, Electrocatalysis. 9 (2018) 47–58, https://doi.org/10.1007/s12678-017-0415-5.

[35] Y. Xu, N. Ullah, L. Chen, W. Wei, C.J. Oluigbo, M. Xie, M. Zhang, J. Xie, Nickel loaded graphene-like carbon sheets an improved electrocatalyst for hydrogen evolution reaction, Mater. Chem. Phys. 227 (2019) 105–110, https://doi.org/10.1016/j.matchemphys.2019.01.066.

[36] C. Wang, Y. Li, X. Wang, J. Tu, N-Doped NiO Nanosheet Arrays as Efficient Electrocatalysts for Hydrogen Evolution Reaction, J. Electron. Mater. 50 (2021) 5072–5080, https://doi.org/10.1007/s11664-021-09053-w.

[37] B. Liu, H. Peng, J. Cheng, K. Zhang, D. Chen, D. Shen, S. Wu, T. Jiao, X. Kong, Q. Gao, S. Bu, C. Lee, W. Zhang, Nitrogen-doped graphene-encapsulated nickel-copper alloy nanoflower for highly efficient electrochemical hydrogen evolution reaction, Small. 15 (2019) 1901545, https://doi.org/10.1002/smll.201901545.

[38] W. Wan, Z. Zhao, H. Hu, Y. Gogotsi, J. Qiu, Highly controllable and green reduction of graphene oxide to flexible graphene film with high strength, Mater. Res. Bull. 48 (2013) 4797–4803, https://doi.org/10.1016/j.materresbull.2013.08.031.

[39] J. Flórez-Montaño, A. Calderón-Cárdenas, W. Lizcano-Valbuena, J.L. Rodríguez, E. Pastor, Ni@Pt nanodisks with low Pt content supported on reduced graphene oxide for methanol electrooxidation in alkaline media, Int. J. Hydrogen Energy. 41 (2016) 19799–19809, https://doi.org/10.1016/j.ijhydene.2016.06.166.

[40] L.M. Rivera Gavidia, G. García, D. Anaya, A. Querejeta, F. Alcaide, E. Pastor, Carbon-supported Pt-free catalysts with high specificity and activity toward the oxygen reduction reaction in acidic medium, Appl. Catal. B Environ. 184 (2016) 12–19, https://doi.org/10.1016/j.apcatb.2015.11.021.

[41] O.F. Er, A. Caglar, B. Ulas, H. Kivrak, A. Kivrak, Novel carbon nanotube supported Co@Ag@Pd formic acid electrooxidation catalysts prepared via sodium borohydride sequential reduction method, Mater. Chem. Phys. 241 (2020) 122422, https://doi.org/10.1016/j.matchemphys.2019.122422.

[42] V. Kumar, A. Kumar, D.-J. Lee, S.-S. Park, Estimation of number of graphene layers using different methods: a focused review, Materials (Basel). 14 (2021) 4590, https://doi.org/10.3390/ma14164590.

[43] B. Partoens, F.M. Peeters, From graphene to graphite: Electronic structure around the K point, Phys. Rev. B. 74 (2006) 075404, https://doi.org/10.1103/PhysRevB.74.075404.

[44] N.L. Alpert, W.E. Keiser, H.A. Szymanski. IR. Theory and Practice of Infrared Spectroscopy, Springer US, Boston, MA, 1970, https://doi.org/10.1007/978-1-4684-8160-0.

[45] L.D. Field, S. Sternhell, J.R. Kalman, Organic structures from spectra, Fourth Edi, Wiley (2008).

[46] J.J. Workman, L. Weyer. Practical Guide to Interpretive Near-Infrared Spectroscopy, 2007, https://doi.org/10.1201/9781420018318.

[47] D. Yoon, H. Cheong, Raman Spectroscopy for Characterization of Graphene, in: Raman Spectrosc. Nanomater. Charact, Springer Berlin Heidelberg, Berlin, Heidelberg, 2012, pp. 191–214, https://doi.org/10.1007/978-3-642-20620-7_9.

[48] C. Botas, P. Álvarez, C. Blanco, R. Santamaría, M. Granda, P. Ares, F. Rodríguez-Reinoso, R. Menéndez, The effect of the parent graphite on the structure of graphene oxide, Carbon N. Y. 50 (2012) 275–282, https://doi.org/10.1016/j.carbon.2011.08.045.

[49] W. Tian, H. Zhang, Z. Qian, T. Ouyang, H. Sun, J. Qin, M.O. Tadé, S. Wang, Bread-making synthesis of hierarchically Co@C nanoarchitecture in heteroatom doped porous carbons for oxidative degradation of emerging contaminants, Appl. Catal. B Environ. 225 (2018) 76–83, https://doi.org/10.1016/j.apcatb.2017.11.056.

[50] W. Du, Q. Zhang, Y. Shang, W. Wang, Q. Li, Q. Yue, B. Gao, X. Xu, Sulfate saturated biosorbent-derived Co-S@NC nanoarchitecture as an efficient catalyst for peroxymonosulfate activation, Appl. Catal. B Environ. 262 (2020) 118302, https://doi.org/10.1016/j.apcatb.2019.118302.

[51] D. Titus, E. James Jebaseelan Samuel, S.M. Roopan, Nanoparticle characterization techniques, in: A.K. Shukla, S.B.T.-G.S. Iravani Characterization and Applications of Nanoparticles (Eds.), Green Synth. Charact. Appl. Nanoparticles, Elsevier, 2019: pp. 303–319. https://doi.org/10.1016/B978-0-08-102579-6.00012-5.

[52] F. Fioravanti, S. Martínez, S. Delgado, G. García, J.L. Rodriguez, E.P. Tejera, G.I. Lacconi, Effect of MoS2 in doped-reduced graphene oxide composites. Enhanced electrocatalysis for HER, Electrochim. Acta. 441 (2023) 141781, https://doi.org/10.1016/j.electacta.2022.141781.

[53] A. Serov, K. Artyushkova, P. Atanassov, Fe-N-C oxygen reduction fuel cell catalyst derived from carbendazim: Synthesis, structure, and reactivity, Adv. Energy Mater. 4 (2014) 1–7, https://doi.org/10.1002/aenm.201301735.

[54] G. Wu, C.M. Johnston, N.H. MacK, K. Artyushkova, M. Ferrandon, M. Nelson, J.S. Lezama-Pacheco, S.D. Conradson, K.L. More, D.J. Myers, P. Zelenay, Synthesis-structure-performance correlation for polyaniline-Me-C non-precious metal cathode catalysts for oxygen reduction in fuel cells, J. Mater. Chem. 21 (2011) 11392–11405, https://doi.org/10.1039/c0jm03613g.

[55] M.M. Hossen, K. Artyushkova, P. Atanassov, A. Serov, Synthesis and characterization of high performing Fe-N-C catalyst for oxygen reduction reaction (ORR) in Alkaline Exchange Membrane Fuel Cells, J. Power Sources. 375 (2018) 214–221, https://doi.org/10.1016/j.jpowsour.2017.08.036.

[56] I. Nancucheo, A. Segura, P. Hernández, C. Canales, N. Benito, A. Arranz, M. Romero-Sáez, G. Recio-Sánchez, Bio-recovery of CuS nanoparticles from the treatment of acid mine drainage with potential photocatalytic and antibacterial applications, Sci. Total Environ. 902 (2023) 166194, https://doi.org/10.1016/j.scitotenv.2023.166194.

[57] J.F.. Moulder, J. Chastain, Handbook of x-ray photoelectron spectroscopy: a reference book of standard spectra for identification and interpretation of XPS data, Eden Prairie, Minn: Physical Electronics Division, Perkin-Elmer Corp. (1992).

[58] S. Fajardo, P. Ocón, J.L. Rodríguez, E. Pastor, Co supported on N and S dual-doped reduced graphene oxide as highly active oxygen-reduction catalyst for direct ethanol fuel cells, Chem. Eng. J. 461 (2023) 142053, https://doi.org/10.1016/j.cej.2023.142053.

[59] K.S. Kim, N. Winograd, X-ray photoelectron spectroscopic studies of nickel-oxygen surfaces using oxygen and argon ion-bombardment, Surf. Sci. 43 (1974) 625–643, https://doi.org/10.1016/0039-6028(74)90281-7.

[60] M.L. Escudero, I. Llorente, B.T. Pérez-Maceda, S.S. José-Pinilla, L. Sánchez-López, R.M. Lozano, S. Aguado-Henche, C.C. de Arriba, M.A. Alobera-Gracia, M.C. García-Alonso, Electrochemically reduced graphene oxide on CoCr biomedical alloy: Characterization, macrophage biocompatibility and hemocompatibility in rats with graphene and graphene oxide, Mater. Sci. Eng. C. 109 (2020) 110522, https://doi.org/10.1016/j.msec.2019.110522.

[61] M.G. Hosseini, F. Hosseinzadeh, P. Zardari, O. Mermer, Pd-ni nanoparticle supported on reduced graphene oxide and multi-walled carbon nanotubes as electrocatalyst for oxygen reduction reaction, fullerenes nanotub, Carbon Nanostructures. 26 (2018) 675–687, https://doi.org/10.1080/1536383X.2018.1465049.

[62] A.P. Grosvenor, M.C. Biesinger, R.S.C. Smart, N.S. McIntyre, New interpretations of XPS spectra of nickel metal and oxides, Surf. Sci. 600 (2006) 1771–1779, https://doi.org/10.1016/j.susc.2006.01.041.

[63] X. Liu, W. Liu, M. Ko, M. Park, M.G. Kim, P. Oh, S. Chae, S. Park, A. Casimir, G. Wu, J. Cho, Metal (Ni, Co)-metal oxides/graphene nanocomposites as multifunctional electrocatalysts, Adv. Funct. Mater. 25 (2015) 5799–5808, https://doi.org/10.1002/adfm.201502217.

[64] Z. Wang, C. Carrière, A. Seyeux, S. Zanna, D. Mercier, P. Marcus, XPS and ToF-SIMS investigation of native oxides and passive films formed on nickel alloys containing chromium and molybdenum, J. Electrochem. Soc. 168 (2021) 041503, https://doi.org/10.1149/1945-7111/abf308.

[65] A. Larsson, G. D'Acunto, M. Vorobyova, G. Abbondanza, U. Lienert, Z. Hegedüs, A. Preobrajenski, L.R. Merte, J. Eidhagen, A. Delblanc, J. Pan, E. Lundgren, Thickness and composition of native oxides and near-surface regions of ni superalloys, J. Alloys Compd. 895 (2022) 162657, https://doi.org/10.1016/j.jallcom.2021.162657.

[66] G. Bhargava, I. Gouzman, C.M. Chun, T.A. Ramanarayanan, S.L. Bernasek, Characterization of the "native" surface thin film on pure polycrystalline iron: a high resolution XPS and TEM study, Appl. Surf. Sci. 253 (2007) 4322–4329, https://doi.org/10.1016/j.apsusc.2006.09.047.

[67] S.L. Medway, C.A. Lucas, A. Kowal, R.J. Nichols, D. Johnson, In situ studies of the oxidation of nickel electrodes in alkaline solution, J. Electroanal. Chem. 587 (2006) 172–181, https://doi.org/10.1016/j.jelechem.2005.11.013.

[68] M. Luis-Sunga, J.L. Rodríguez, G. García, E. Pastor, Oxygen electroreduction reaction at bidimensional materials, Curr. Opin. Electrochem. 23 (2020) 139–144, https://doi.org/10.1016/j.coelec.2020.05.015.

[69] F. Si, Y. Zhang, L. Yan, J. Zhu, M. Xiao, C. Liu, W. Xing, J. Zhang. Electrochemical Oxygen Reduction Reaction, Elsevier B.V, 2014, https://doi.org/10.1016/B978-0-444-63278-4.00004-5.

[70] M.H. Kim, Y.A. Kang, I.Y. Jeon, Oxygen reduction reaction by metal-free catalysts, Elsevier Inc., 2022, https://doi.org/10.1016/B978-0-323-88508-9.00007-0.

[71] P.K. Shen, Electrochemical oxygen reduction, Springer Singapore, Singapore, 2021, https://doi.org/10.1007/978-981-33-6077-8.

[72] Y. Pradesar, A. Yusuf, D.M. Kabtamu, H.C. Huang, C.H. Wang, Nickel-cobalt metal-organic framework CPO-27 and g-C3N4 for oxygen reduction reaction in alkaline-exchange-membrane fuel cell, ACS Appl. Energy Mater. (2023), https://doi.org/10.1021/acsaem.3c00589.

[73] J.C.C. Gómez, R. Moliner, M.J. Lázaro, Palladium-based catalysts as electrodes for direct methanol fuel cells: a last ten years review, Catalysts. 6 (2016), https://doi.org/10.3390/catal6090130.

[74] A.J. Bard, L.R. Faulkner, Electrochemical methods. fundamentals and applications, second edi, John Wiley & Sons, 2001.

[75] S. Sun, H. Li, Z.J. Xu, Impact of Surface Area in Evaluation of Catalyst Activity, Joule. 2 (2018) 1024–1027, https://doi.org/10.1016/j.joule.2018.05.003.

[76] S. Gottesfeld, Electrocatalysis of oxygen reduction in Polymer electrolyte fuel cells: a brief history and a critical examination of present theory and diagnostics, in: Fuel Cell Catal, John Wiley & Sons Inc, Hoboken, NJ, USA, 2008, pp. 1–30, https://doi.org/10.1002/9780470463772.ch1.

[77] G. Pérez, E. Pastor, C.F. Zinola, A novel Pt/Cr/Ru/C cathode catalyst for direct methanol fuel cells (DMFC) with simultaneous methanol tolerance and oxygen promotion, Int. J. Hydrogen Energy. 34 (2009) 9523–9530, https://doi.org/10.1016/j.ijhydene.2009.09.088.

[78] S. Fletcher, Tafel slopes from first principles, J. Solid State Electrochem. 13 (2009) 537–549, https://doi.org/10.1007/s10008-008-0670-8.

[79] Y. Hao, Y. Xu, J. Liu, X. Sun, Nickel-cobalt oxides supported on Co/N decorated graphene as an excellent bifunctional oxygen catalyst, J. Mater. Chem. a. 5 (2017) 5594–5600, https://doi.org/10.1039/c7ta00299h.

[80] T.J. Schmidt, H.A. Gasteiger, G.D. Stäb, P.M. Urban, D.M. Kolb, R.J. Behm, Characterization of high-Surface-area electrocatalysts using a rotating disk electrode configuration, J. Electrochem. Soc. 145 (1998) 2354–2358, https://doi.org/10.1149/1.1838642.

[81] O.A. Petrii, E. Chemistry, And electrochemical applications | hydrogen, In: Encycl. Electrochem. Power Sources, Elsevier (2009) 751–761, https://doi.org/10.1016/B978-044452745-5.00868-6.

[82] S. Díaz-Coello, G. García, M.C. Arévalo, E. Pastor, Precise determination of tafel slopes by DEMS. hydrogen evolution on tungsten-based catalysts in alkaline solution, Int. J. Hydrogen Energy. 44 (2019) 12576–12582, https://doi.org/10.1016/j.ijhydene.2019.02.151.

[83] J. Huang, Diffusion impedance of electroactive materials, electrolytic solutions and porous electrodes: Warburg impedance and beyond, Electrochim. Acta. 281 (2018) 170–188, https://doi.org/10.1016/j.electacta.2018.05.136.

[84] S. Cruz-Manzo, I. Martínez-Zárate, Analytical transfer function for the simulation of the frequency-domain and time-domain responses of the blocked-diffusion Warburg impedance, J. Energy Storage. 72 (2023) 108676, https://doi.org/10.1016/j.est.2023.108676.

[85] J.-S. Kim, S.-I. Pyun, Comparison of transmissive permeable and reflective impermeable interfaces between electrode and electrolyte, J. Solid State Electrochem. 15 (2011) 2447–2452, https://doi.org/10.1007/s10008-011-1393-9.

[86] S. Delgado, Y. Remedios-Díaz, J.C. Calderón, S. Díaz-Coello, M.C. Arévalo, G. García, E. Pastor, Catalytic activity of 2D MXenes toward electroreduction processes: oxygen reduction and hydrogen evolution reactions, Int. J. Hydrogen Energy. (2023), https://doi.org/10.1016/j.ijhydene.2023.11.288.